How to cite: *Angew. Chem. Int. Ed.* **2023,** *62,* e202303111
doi.org/10.1002/anie.202303111

Li-Ion Batteries

Overcoming Diffusion Limitation of Faradaic Processes: Property-Performance Relationships of 2D Conductive Metal-Organic Framework $Cu_3(HHTP)_2$ for Reversible Lithium-Ion Storage

Jens Matthies Wrogemann[+], Marco Joes Lüther[+], Peer Bärmann, Mailis Lounasvuori, Ali Javed, Michael Tiemann, Ronny Golnak, Jie Xiao, Tristan Petit, Tobias Placke,* and Martin Winter*

Abstract: Faradaic reactions including charge transfer are often accompanied with diffusion limitation inside the bulk. Conductive two-dimensional frameworks (2D MOFs) with a fast ion transport can combine both—charge transfer and fast diffusion inside their porous structure. To study remaining diffusion limitations caused by particle morphology, different synthesis routes of Cu-2,3,6,7,10,11-hexahydroxytriphenylene ($Cu_3(HHTP)_2$), a copper-based 2D MOF, are used to obtain flake- and rod-like MOF particles. Both morphologies are systematically characterized and evaluated for redox-active Li^+ ion storage. The redox mechanism is investigated by means of X-ray absorption spectroscopy, FTIR spectroscopy and in situ XRD. Both types are compared regarding kinetic properties for Li^+ ion storage via cyclic voltammetry and impedance spectroscopy. A significant influence of particle morphology for 2D MOFs on kinetic aspects of electrochemical Li^+ ion storage can be observed. This study opens the path for optimization of redox active porous structures to overcome diffusion limitations of Faradaic processes.

Introduction

Lithium-ion batteries (LIBs) are used as energy storage technology to solve the intermittency issues of renewable energy sources due to their long cycle life and high round-trip/energy efficiency.[1] Since then, high cost and growing environmental concerns linked mainly to state-of-the-art (SOTA) cathode active materials (CAMs) based on layered transition metal oxides has inspired researchers to look for alternative energy storage materials.[2] In parallel, recent advances in the design of electronically conductive metal–organic frameworks (c-MOFs)[3] pave the way to introduce the benefits of MOFs (e.g., size-tunable porosity, variable functionality, regularly spaced active centers) to areas of research where their electronically insulating nature had previously hindered application (e.g., energy conversion,[4] electrocatalysis,[4a,5] electronics,[5b,6] sensing[5b,7] and energy storage[8]). Due to the development of MOFs with promising electrochemical properties, MOFs gained more and more attraction as functional material for energy storage in the last years.[9]

The subclass of 2D c-MOFs has been identified as a good match for battery applications as insertion/intercalation-type active materials. The use of flat, π-conjugated ligands that are able to coordinate transition metals in a planar geometry with multiple bidentate functional groups leads to the formation of layered sheet structures with extraordinarily high conductivity.[3] Regular channels (perpendicular to the sheets) enable fast transport of metal ions to the redox active sites within the material while the flexibility of the structure (layers are only connected by π–π-interactions) allows for their accommodation.[10] The successful use of 2D c-MOFs in LIBs was first reported in 2018 by Wada et al.[11] With $Ni_3(HIB)_2$ (HIB = hexaiminobenzene) as the CAM in a Li-metal cell setup; the authors

[*] J. M. Wrogemann,[+] M. J. Lüther,[+] Dr. T. Placke, Prof. M. Winter
University of Münster, MEET Battery Research Center
Corrensstraße 46, 48149 Münster (Germany)
E-mail: jwrogemann@uni-muenster.de
tobias.placke@uni-muenster.de
Dr. P. Bärmann, Dr. M. Lounasvuori, Dr. R. Golnak, Dr. J. Xiao, Dr. T. Petit
Helmholtz-Zentrum Berlin für Materialien und Energie GmbH (HZB)
Albert-Einstein-Straße 15, 12489 Berlin (Germany)
Dr. A. Javed, Prof. M. Tiemann
Paderborn University, Department of Chemistry
Warburger Str. 100, 33098 Paderborn (Germany)
Prof. M. Winter
Helmholtz Institute Münster, IEK-12, Forschungszentrum Jülich GmbH
Corrensstraße 46, 48149 Münster (Germany)
[+] These authors contributed equally to this work.

achieved a specific capacity of 155 mAh g^{-1} (at 10 mA g^{-1}) and a stable cycling performance over 300 cycles even at 250 mA g^{-1}. The high specific capacity was attributed in part to the redox activity of the linker, which could be reduced and oxidized to balance the charge of both intercalated Li^+-cations and anions, respectively. A study of the copper analogue $Cu_3(HIB)_2$ again confirmed the involvement of both Cu^{II} centers and the linker molecules in the redox activity demonstrating specific capacities of close to 200 mAh g^{-1} after 20 cycles at 5 mA g^{-1}.[12] A comprehensive investigation of this type of charge storage mechanism was performed on $Cu_3(THQ)_2$ (THQ = tetrahydroxy-1,4-benzoquinone) by Jiang et al.[13] who were able to demonstrate the redox activity of the metal center and linker by UV-Vis spectroscopy and electron paramagnetic resonance spectroscopy (EPR) studies, respectively. In addition, the specific capacity and cycling stability (340 mAh g^{-1} after 100 cycles at 50 mA g^{-1}) are unparalleled for 2D c-MOFs.

Another interesting member of the 2D c-MOF class is $Cu_3(HHTP)_2$ (HHTP = 2,3,6,7,10,11-hexahydroxytriphenylene)—one of the most thoroughly explored members of the 2D c-MOF family. $Cu_3(HHTP)_2$ has attracted interest for use in electrochemical applications due to (i) its straightforward synthesis from commercially available reagents, (ii) its large pore diameter which is believed to facilitate the transport of Li^+ to its electrochemically active centers, as well as (iii) the absence of critical elements such as Co and Ni, which makes it a promising alternative electrode material.[2] $Cu_3(HHTP)_2$ was first synthesized in 2012 by Hmadeh et al.[14] through hydrothermal treatment of an aqueous dispersion comprising copper salt and protonated linker. After measuring a conductivity of 0.21 S cm^{-1} (single crystal), the authors revealed a Li^+ ion storage capacity of 80 mAh g^{-1} after 50 cycles.[14] These first promising results convinced other researchers to apply $Cu_3(HHTP)_2$ in the field of solid-state supercapacitors,[15] photovoltaics[16] and sensing[17] even though its conductivity was shown to be lower in thin films (0.001–0.02 S cm^{-1})[18] or as pressed pellets (0.002–0.027 S cm^{-1}).[16,17b] Nam et al. also applied the Cu-MOF as an active material in aqueous zinc batteries showing a discharge capacity of 228 mAh g^{-1} at a current of 50 mA g^{-1}. As in previous examples, the capacity was partly attributed to the redox activity of the linker.[19] Remarkably, $Cu_3(HHTP)_2$ was able to retain quite a high fraction of its capacity at higher currents and proved to be stable during cycling. At a current of 500 mA g^{-1}, the Cu-MOF showed an initial capacity of 152 mAh g^{-1} and maintained 75 % of this capacity after 100 cycles. Even at 4000 mA g^{-1}, a similar retention was reached after 500 cycles with only a slightly diminished initial capacity of 124 mAh g^{-1}. Intrigued by this, the authors investigated the kinetics of charge storage in $Cu_3(HHTP)_2$ by performing cyclic voltammetry (CV) experiments at varying scan rates. They concluded that the origin of the high rate capability was a "pseudo-capacitive" charge-storage mechanism in which a Faradaic reaction (e.g., insertion of cations coupled with charge transfer) occurs so fast that it can be described with the mathematical models of non-Faradaic reactions (e.g., electric double layer formation).[20] The high-rate capability of $Cu_3(HHTP)_2$ had also been previously observed by Gu et al. who evaluated this material in a LIB cell with currents between ≈50 mA g^{-1} and ≈2000 mA g^{-1}. While they obtained lower initial capacity, the capacity retention was enhanced at higher currents reaching 85 % after 500 cycles at ≈2000 mA g^{-1}.[21] It is well known that kinetics of electrochemical reactions are highly dependent on surface properties of investigated materials.[22] The surface of 2D c-MOFs is mostly determined by their particle morphology and crystal structure. However, there are no systematic studies about the impact of the particle morphology of MOFs so far. For $Cu_3(HHTP)_2$, the electrochemical kinetics of Li^+ ion storage inside the porous structure remains particularly unclear.

In this study, we investigate the relationship between particle morphology, surface area and kinetics of ion storage for 2D c-MOFs $Cu_3(HHTP)_2$. To the best of our knowledge, these relationships of ion storage and material properties for 2D MOFs are investigated for the first time in this study. For this purpose, $Cu_3(HHTP)_2$ 2D c-MOFs with two radically different particle morphologies—rod-like and flake-like—are synthesized. First, both materials are characterized with X-ray diffraction (XRD), thermalgravimetric analysis (TGA), scanning electron microscopy with energy-dispersive X-ray spectroscopy (SEM-EDX) and gas physisorption measurements. Furthermore, infrared spectroscopy (FTIR), soft X-ray absorption spectroscopy (sXAS) and XRD experiments are employed along with electrochemical methods to unravel the charge storage mechanism of $Cu_3(HHTP)_2$. Finally, electrochemical properties based on constant current charging, CV experiments and stepped potential electrochemical impedance spectroscopy (SPEIS) are analyzed for two different morphologies to reveal property-performance relationships with implications for the whole class of 2D c-MOFs.

Results and Discussion

MOFs can be synthesized in different ways. The most common procedure is a solvothermal synthesis by heat treatment of a solution consisting of a solvent, metal precursor, solved linker molecule, and possible additives in a closed system.[23] It is well-known that the reaction parameters like educts, temperature, concentration, additives, pressure, and others can have a strong impact on the physical properties, e.g. crystallinity and morphology, of the product.[23,24] For the synthesis of $Cu_3(HHTP)_2$, several synthesis procedures and parameters have been investigated in literature to understand the chemistry of the reaction. Day et al. demonstrated via TEM investigations of single-crystal specimen, that the crystal growth proceeds preferably parallel to the crystallographic *c*-direction (supposedly due to the π–π-interactions of the hydrophobic linker core). Hence, $Cu_3(HHTP)_2$ usually presents in a rod-like morphology where these pores are oriented parallel to the long axis.[25] Hoppe et al. managed to redirect the crystal growth in a lateral direction by employing ammonia in the solution

as a so-called "modulator" to obtain thin, flake-like particles with the pores oriented perpendicular to their faces.[17a] Considering ion storage in these open structures, this change in morphology should drastically enhance pore accessibility as the length of the pores is reduced from micro- to nano-size, while the number of pore openings at the particle surface is drastically increased.[17a,25] For the purpose of this study, published synthesis procedures[16,17] were slightly modified and adapted (see experimental part, Supporting Information) to synthesize $Cu_3(HHTP)_2$ in two characteristically distinct morphologies, which throughout this work will be referred to as rod-like (rods) and flake-like (flakes) $Cu_3(HHTP)_2$, respectively. Figure 1 shows scanning electron microscopy (SEM) images of both synthesized products—rod-like particles of several micrometers in length (Figure 1a) as well as nanometer-thin flake-like particles (Fig-

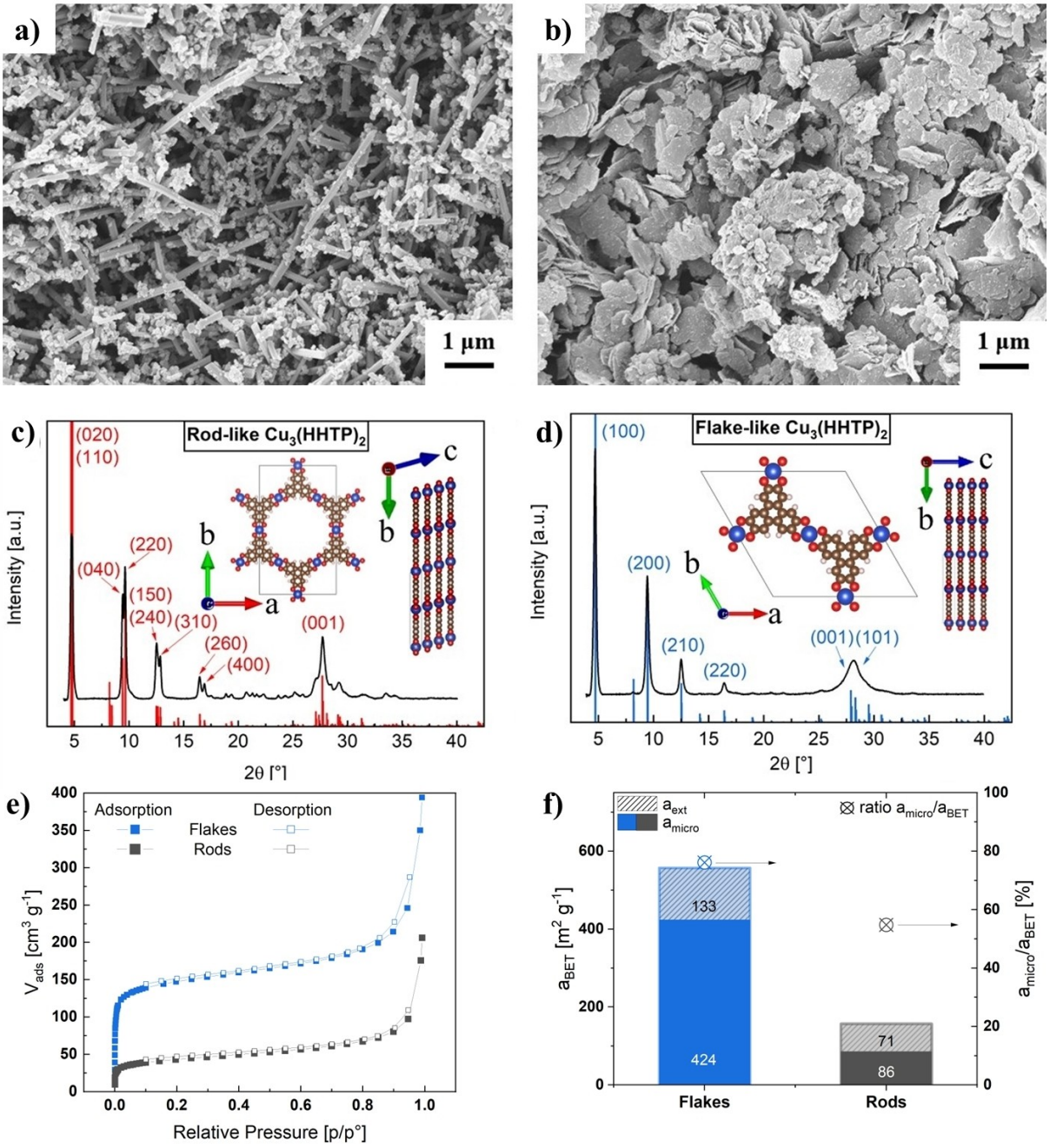

Figure 1. Characterization of rod-like and flake-like $Cu_3(HHTP)_2$: a), b) SEM images of (a) rod-like and (b) flake-like $Cu_3(HHTP)_2$. c), d) Experimental (black line) and modelled PXRD data (red/blue lines) including schematics of the crystallographic model (Cu = blue, C = brown, O = red, H = white) for (c) rod-like $Cu_3(HHTP)_2$ and (d) flake-like $Cu_3(HHTP)_2$. e), f) Physisorption data for rod-like (grey) and flake-like $Cu_3(HHTP)_2$ (blue) after an activation step at 60 °C under reduced pressure ($p < 0.05$ mbar) for 20 h, showing (e) N_2 physisorption isotherms and (f) total surface area a_{BET}, microporous surface area a_{micro} and external surface area a_{ext} (bar chart, left *y*-axis) as well as contribution of micropores (a_{micro}/a_{BET}, right *y*-axis). a_{BET} is a sum of a_{micro} and a_{ext}. Numbers written in bar chart (f) corresponds to the values of a_{micro} and a_{ext} for each morphology.

ure 1b). Focusing on the rod-like particles in Figure 1a, some rods are partly covered with tiny hump-like structures, which might be small outgrowing MOF-structures caused by tremendous upscaling (10 to 30-fold) of synthesis procedure or high sensitivity towards the surface, on which the MOF starts to growth.[15,16] Nevertheless, the rod-like morphology is highly dominant.

EDX measurements confirmed that the elemental composition of both materials is very close to the theoretically expected values (Table S1). The successful synthesis was further verified by powder X-ray diffraction (PXRD) measurements showing characteristic reflections at low 2θ angles associated with the large repeating units in the MOF structure (Figure 1c,d). Surprisingly, the two materials showed slightly different PXRD patterns. Most notably, a splitting of some reflections is observed for rod-like $Cu_3(HHTP)_2$ as opposed to its flake-like analogue. Because the crystal structure of $Cu_3(HHTP)_2$ has not yet been finally determined, crystallographic models of the layered MOF structure were constructed with VESTA[26] to enable further interpretation of the PXRD data (Figure S1 and Table S2). It is widely believed that—analogous to other 2D c-MOFs—$Cu_3(HHTP)_2$ is comprised of regular hexagonal sheets, in which each copper atom is coordinated in a planar manner by four oxygen atoms of two different linker molecules. Comparison to simulated PXRD data shows that these sheets are perfectly aligned for flake-like $Cu_3(HHTP)_2$ (eclipsed stacking),[17a] whereas they have to be stacked with a constant shift for its rod-like analogue (tilted stacking).[25] The resulting loss of symmetry (from a hexagonal to a monoclinic space group) can explain the additional reflections observed for rod-like $Cu_3(HHTP)_2$. While the crystallographic models matched the observed reflection positions quite well, the intensity ratios between different reflections could not be reproduced. On this basis, a LeBail refinement[27] of the PXRD data was performed (Figure S2) to finetune the model, index the reflections and determine the unit cell dimensions. In Figure 1c,d, the experimental PXRD data is compared to data generated from this model.

The refined XRD pattern is deliberately not shown here, as it might give a false sense of the accuracy of the crystallographic model, but the complete refinement results can be found in the Supporting Information (Figure S3, Table S3). More research is needed to determine the crystal structure of $Cu_3(HHTP)_2$ precisely. Nevertheless, the results show that $Cu_3(HHTP)_2$ has regular hexagonal pores with a diameter of about 2.16 nm which agrees well with literature.[16,17,25,28]

With an open pore system as described, guest molecules (e.g., solvents from the synthesis) may be trapped in the material unintentionally which may inhibit pore accessibility.[29] These guest molecules can be removed by careful heat treatment under reduced pressure, often referred to as an "activation step". Since there are conflicting reports on the thermal stability of $Cu_3(HHTP)_2$,[17a,21] samples of $Cu_3(HHTP)_2$ were activated at temperatures ranging from room temperature (RT), 60 °C, 80 °C, 100 °C up to 120 °C. Subsequently, TGA (Figure S4, S5) and PXRD measurements (Figure S6) were employed to investigate the removal of guest molecules and its effect on the crystal structure. In an atmosphere of pure oxygen, $Cu_3(HHTP)_3$ combusts at elevated temperatures leaving only CuO behind as determined by PXRD (see Figure S5b). This enables the estimation of the amount of guest molecules from TGA data (Table S4). It was shown that after an activation at RT 12 w % of guest molecules are still left in the material while increasing the temperature to 120 °C leads to a lowered amount of guest molecules of 1 wt % (compare Table S4). However, at temperatures higher than 60 °C, the intensity of the reflections, especially the (*100*) reflection at ≈4.8° 2θ decrease with increasing temperatures, indicating a loss of crystallinity (compare Figure S6). As a trade-off between crystallinity and guest removal, 60 °C was chosen as appropriate activation temperature.

The pore accessibility was further probed with nitrogen physisorption experiments (Figure S7). The physisorption isotherms of both rod-like and flake-like $Cu_3(HHTP)_2$ after degassing (60 °C) are illustrated in Figure 1e,f. Both isotherms show a steep increase at low relative pressures ($p/p^0 < 0.005$) transitioning into a quasi-plateau which is indicative of microporosity ($d_{micro} < 2$ nm) as expected from the crystal structure.[30] Using the *t*-plot method (Figure S8 and discussion in Supporting Information), the surface area provided by micropores (a_{micro}) and so called external (non-microporous) surface area (a_{ext}) can be determined, as well as its contribution to the total surface area, given by the BET method.[31] Figure 1f shows the BET surface area (a_{BET}) as well as the contribution of the microporous surface area (a_{micro}/a_{BET}) in both absolute and relative terms for rod-like and flake-like $Cu_3(HHTP)_2$, respectively. Generally, the total accessible surface area of flake-like $Cu_3(HHTP)_2$ is significantly higher compared to the rod-like MOF. After degassing at 60 °C, overall BET surface areas (a_{BET}) of 557 $m^2 g^{-1}$ and 157 $m^2 g^{-1}$ were determined for flake-like and rod-like $Cu_3(HHTP)_2$, respectively (see Figure 1f). A generally higher specific surface area of flake-like particles is observed for different degassing and activation temperatures (see Figure S7, S8 and S9). The maximum value of 245 $m^2 g^{-1}$ for rod-like $Cu_3(HHTP)_2$ was achieved after degassing at 100 °C, the maximum value of 575 $m^2 g^{-1}$ for flake-like MOF was achieved after degassing at 80 °C (see Figure S9), which in line with literature known values (306 $m^2 g^{-1}$).[16] The small deviation might be caused by defects and small fractions of non-perfect morphologies described in an earlier section (compare Figure 1a). For both samples, the overall accessible surface area (a_{BET}) reaches a maximum with increasing temperature and then decreases again. This can be explained by two counteracting effects: while higher temperature facilitates the removal of volatile guest molecules freeing up pore volume, it also causes a degradation of the crystal structure, thus destroying the regular hexagonal pores. This observation is in line with PXRD and TGA results. Although a higher surface area is achieved at degassing temperatures higher than 60 °C, the drying temperatures of all investigated electrodes were fixed to 60 °C due to the loss of crystallinity at higher temperatures.

One could assume that the substantial difference in surface area between the two morphologies can simply be explained by the higher surface-to-volume ratio of the (nanometer-thin) flake-like particles as compared to their (micrometer-long) rod-like counterparts. However, the high a_{micro}/a_{BET} ratios reveal that for both samples, a major part of surface area is provided by micropores inside the structure, meaning that pore accessibility is the decisive factor. To explain why this is the case, the relationship between crystal orientation and pore accessibility needs to be discussed. A simple pore model reveals that the diameter of the micropores in both samples matches well with the diameter of the regular hexagonal channels within their crystal structure, as calculated from PXRD data (see Figure S1, S8 and discussion in Supporting Information). In other words, the hexagonal channels in the crystal structure are the micropores which constitute most of the surface area. TEM investigations on $Cu_3(HHTP)_2$ by other researchers revealed that due to the growth direction of crystals, these hexagonal channels are oriented parallel to the long axis of the rod-like particles, whereas for the flake-like particles their orientation is perpendicular to the particle faces. Therefore, this change in morphology should drastically enhance pore accessibility as the length of the pores is reduced from micro- to nano-size and at the same time, the number of pore openings at the particle surface is increased significantly.[17a,25] These findings match well with the results of the physisorption experiments shown here, considering the total surface area a_{BET} as well as the fraction of microporous surface area a_{micro}/a_{BET} are consistently and significantly higher for flake-like particles. We conclude that the flake-like morphology offers an enhanced pore accessibility as compared to the rod-like morphology. This becomes important when $Cu_3(HHTP)_2$ is employed as an energy storage material because the transport of Li^+ ions to the active sites in the material is likely facilitated by the regular channels within the crystal structure. Thus, an enhanced accessibility of these channels could enable an improved capacity retention at faster (dis)charging rates.

In this regard, electronic conductivity is another important material property. Several two-probe methods using direct and alternating current were employed to measure the electronic conductivity and investigate the electronic transport mechanism within the material (Table S5, Figure S10). It was found that morphology did not affect electronic conductivity significantly and that the charge transport mechanism was the same for both samples. An electronic conductivity of $1.50(3)\times10^{-2}\,S\,cm^{-1}$ was measured which is well within the range of literature results (2×10^{-3}–$1\times10^{-1}\,S\,cm^{-1}$).[16,17,25]

Considering the theoretical specific capacity of $Cu_3(HHTP)_2$, a possible redox activity of both, the copper center and the linker can be assumed. Admittedly, this is not trivial as the precise oxidation and bonding state within these 2D c-MOFs is not yet fully understood.[32] It can be proposed, that during the chemical reaction, the linker undergoes deprotonation and has to be partly oxidized to a semiquinone as opposed to a catecholate (no oxidation) or a quinone (complete oxidation) to maintain charge neutrality (Figure 2a).[33]

Based on these assumptions, $Cu_3(HHTP)_2$ can theoretically take up three electrons per copper center, when Cu^{2+} is reduced to Cu^+ and the linker is changed from its semiquinone to its catecholate form (Figure 2a). The theoretical specific Li^+ ion storage capacity ($Q_{Li,theo.}$) can be calculated according to

$$Q_{Li,theo.} = \frac{1}{M} xzF \quad (1)$$

where $M = 833.22\,g\,mol^{-1}$ is the molar mass of $Cu_3(HHTP)_2$, $x = 3$ is the number of copper atoms per formula unit, z is the number of electrons exchanged per copper atom and $F = 96\,485\,C\,mol^{-1}$ is the Faraday constant. For $z = 1$, 2 and 3, the theoretical capacities are 96.5, 193 and $289.5\,mAh\,g^{-1}$, respectively.

To practically investigate the electrochemical activity, both synthesized morphologies were incorporated in composite electrodes, and CV experiments in a three-electrode half-cell setup with Li metal as the counter and reference electrode, respectively, were conducted (see experimental part in Supporting Information). SEM images and XRD measurements of the electrodes in Figure S11 and S12 demonstrate that the morphology and crystal structure is still dominant after electrode processing. 1 M LiTFSI in EC:EMC (3:7) was used as an electrolyte mixture to suppress possible acidic decomposition of the material. Initial cycling and subsequent XRD experiments showed a stronger degradation and reduced stability in $LiPF_6$-based electrolytes than in a LiTFSI-based composition, which could be caused by water residues inside the porous MOF structure leading to HF formation and an ongoing decomposition of the MOF structure (see Figure S13). Previous CV experiments were conducted in different potential windows to find the window with highest reversibility (see Figure S14 and S15). It could be shown that the potential window between 1.7 V and 3.5 V vs. $Li|Li^+$ leads to the highest Coulombic efficiency (C_{Eff}) and most stable cycling behavior for both morphologies, which is in line with proposed windows in literature.[21] At potentials below 1.2 V vs. $Li|Li^+$ a significant irreversible reductive process seems to start (compare Figure S15), which drastically reduces the C_{Eff} and leads to a decrease of the reversible capacity. The same is true for higher oxidative potentials. Increasing the higher cut-off leads to an initial increase in capacity, however, decreases the reversibility of the reaction (see Figure S14). As a result, the potential window between 1.7 V–3.5 V vs. $Li|Li^+$ was chosen, which leads to a specific capacity of $\approx 100\,mAh\,g^{-1}$ for the flake-like and $90\,mAh\,g^{-1}$ for the rod-like MOFs at a scan rate of $0.5\,mV\,s^{-1}$. Considering the theoretical assumptions made, the reversible redox activity seems to be caused by one electron per formula unit.

To shed light on the lithiation and de-lithiation mechanism of $Cu_3(HHTP)_2$, sXAS and FTIR spectroscopy were employed to distinguish between the redox activity of the Cu species and linker. Since the origin of redox activity of

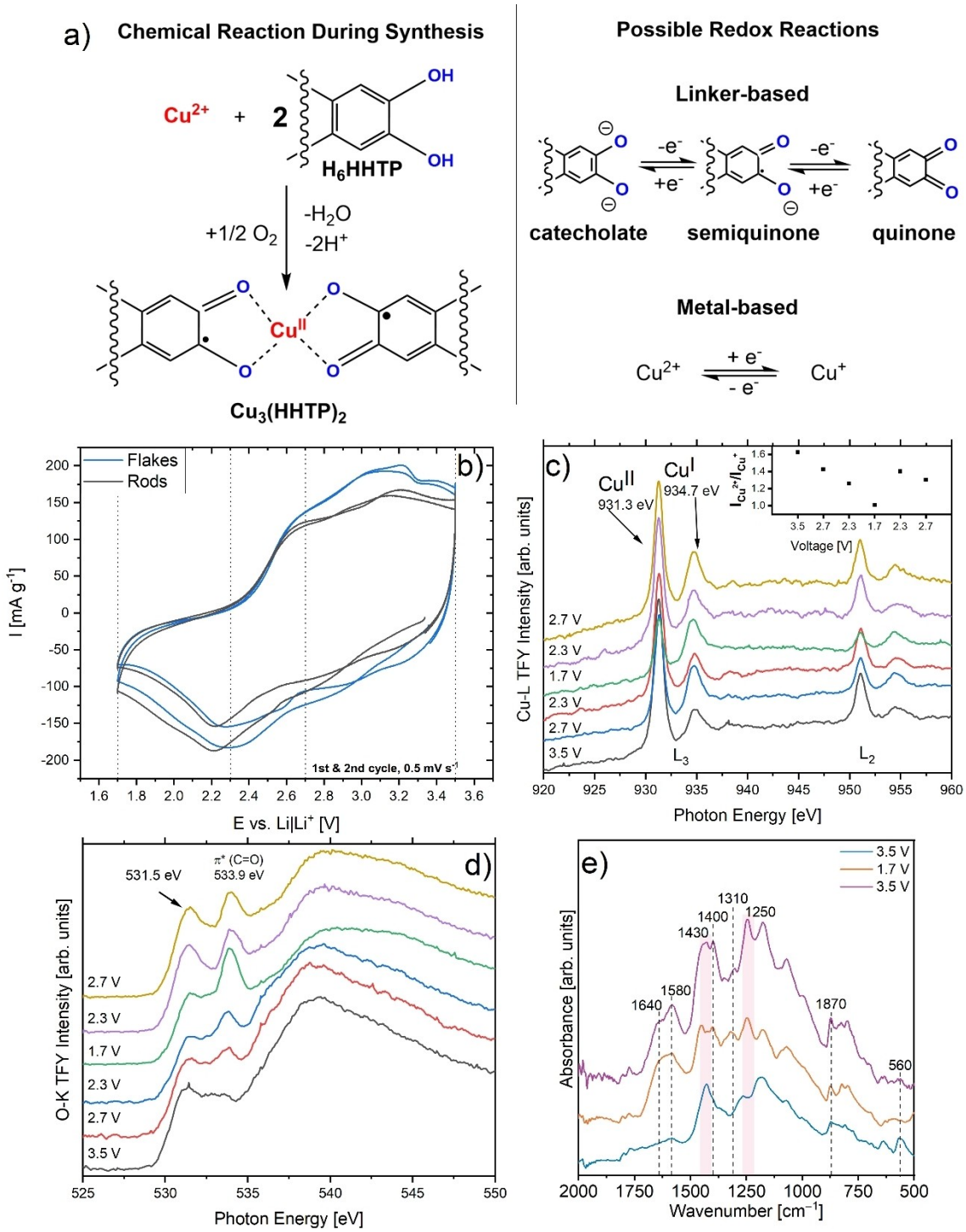

Figure 2. Chemical structure and possible lithiation mechanism of $Cu_3(HHTP)_2$ probed via ex situ sXAS and FTIR spectroscopy. a) Proposed reaction equation for synthesis of $Cu_3(HHTP)_2$ assuming charge neutrality and oxygen as oxidant (top) and possible redox activity of deprotonated linker $HHTP^{6-}$ molecule and coordinated copper during lithiation and de-lithiation (bottom). The complete semiquinoid form $HHTP^{\bullet 3-}$ is a monoradical as opposed to a triradical, because two unpaired electrons can readily combine through the conjugated network.[33b] b) Cyclic voltammetry of $Cu_3(HHTP)_2$ -based electrodes with different morphologies. Due to similarity of the reduction and oxidation pattern only flake-like MOFs were used for further mechanistic studies. Ex situ sXAS of c) Cu $L_{2,3}$-edge and d) O-K-edge as well as e) FTIR spectra of galvanostatic lithiated/de-lithiated of 2nd cycle from flake-like $Cu_3(HHTP)_2$||Li metal cells (two-electrode configuration; voltage range: 1.7–3.5 V vs. Li|Li^+), which are disassembled at distinctive voltages in the 2nd cycle. sXAS are recorded in Total Fluorescence Yield (TFY) mode and are offset in (c) and (d) for clarity. These voltages are marked in Figure 2b for clarification. The inset in Figure 2c displays the intensity ratio of Cu^{2+}/Cu^+ at the L_3 edge as a qualitative indicator for the changing oxidation state of the Cu species.

two isomeric structures with the same composition but different morphology should not differ, only the flake type was representatively investigated. sXAS is especially suited to identify the Cu oxidation state and bonding environment since it allows to probe the electronic structure of the redox active material with element-specificity (Cu L and O K-edge, Figure 2c and d, respectively). sXAS was conducted in the fluorescence yield mode to probe the bulk ($\approx$100 nm)[34] material and thereby ruling out any influence of surface contaminants such as residual electrolyte components. The spin-orbit coupling induces a splitting of the Cu L-edge XA spectra (hence L_2 and L_3, Figure 2c) which are themselves split into two peaks (934.7 eV and 931.3 eV for the L_3-edge) due to different oxidation state and coordination environment of the copper atoms. The absorption peaks at 934.7 eV and 931.3 eV are assigned to the Cu^+ and Cu^{2+} oxidation state by comparison to cuprous and cupric oxide, respectively.[35] These differences are a result of the close and open 3d shell structure of Cu^+ and Cu^{2+}, respectively, which allows to qualitatively compare the oxidation state of the copper species between the investigated samples.[36]

The de-lithiated sample (black curve, Figure 2c, 3.5 V) displays no clear difference to the pristine sample (Figure S16a), proving the electrochemical stability of the active material after the first cycle (1.7–3.5 V). The majority of the copper species is found in the Cu^{2+} state. The residual Cu^+ species are already formed during synthesis (Figure S16a) and therefore not due to electrochemical cycling. The intensity ratio between the Cu^{2+} and Cu^+ species decreases during lithiation (Figure 2c, from 3.5 V to 1.7 V) therefore proving the reduction of the copper species during lithiation (inset in Figure 2c). However, Cu^{2+} species are still detectable at the lowest voltage of 1.7 V (highest lithiation), demonstrating the incomplete lithiation of the underlying active material. Upon de-lithiation, the intensity ratio increases again, indicating the successful oxidation of the copper species. All in all, these results prove the reversible redox activity of the copper species.

To investigate the role of the linker on the overall electrochemical activity and stability of $Cu_3(HHTP)_2$, the evolution of the ex situ sXAS at the O-K edge acquired at different voltages was examined (Figure 2d). In the pre-edge region ($<$535 eV), electronic transitions from the O 1s to the hybridized O 2p/Cu 3d (e_g) orbitals and from the O 1s to the π^* antibonding orbitals of C=O/C–O bonds were probed, allowing to monitor the redox activity of the oxygen containing species of the MOF.[13,34,37]

Before lithiation (Figure 2d, 3.5 V), the O-K pre-edge is missing a clear absorption peak (531.2 eV) associated with the Cu–O bond, which is observable in the pristine sample (Figure S16b) indicating irreversible reactions occurring during the first cycle. During lithiation, a new absorption peak emerges at 533.9 eV with limited reversibility, which is associated with transition to π^* state from the C=O bonds. The energy of the transition is heavily influenced by the bond-bond interaction from the phenyl π^* density, which can make a clear interpretation of data difficult.[38] Additionally, during de-lithiation, another absorption peak at 531.5 eV emerges, which has been previously linked to Li–O bonds during the lithiation of copper-benzoquinoid,[13] but could also be due to other oxygen-containing species. Both peaks exhibit limited reversibility and therefore could be due to other occurring side reactions such as irreversible oxidation of the copper species.

To further resolve the nature of the oxygen bonding upon (de-)lithiation, ex situ FTIR spectroscopy was conducted (Figure 2e). Infrared spectroscopy can discriminate between semiquinone and catecholate complexes due to the C–O stretch vibration that redshifts with increased reduction of the ligand.[39] The reference spectrum of the Cu-MOF (Figure S17a) shows the semiquinone band at $\approx$1430 cm^{-1} characteristic of metal-semiquinone complexes. This band is also present in the de-lithiated sample as expected. In the lithiated electrode spectrum, the semiquinone band loses intensity and a new band at 1250 cm^{-1} appears, which could relate to the C–O stretch band of metal-catecholate complexes (Figure 2e).[39] The semiquinone is hence reduced to catecholate, indicating that the linker is redox active during lithiation. The band at 1580 cm^{-1} is assigned to a ring mode that is nearly absent from Cu–MOF and the de-lithiated sample due to lack of conjugation in the ring.[13] An increased intensity of the C=O stretching band at 1640 cm^{-1} is also observed, in agreement with the XAS at the O-K-edge. This peak may relate to further reduction of the catecholate to a quinone or arise from an electrolyte decomposition product such as $ROCO_2Li$ species, which would also explain the peak at 1310 cm^{-1}.[40] Electrolyte decomposition products in the form of $ROCO_2Li$ (1640 cm^{-1}, 1310 cm^{-1}) and Li_2CO_3 (1400 cm^{-1}, 870 cm^{-1}) have been reported on Sn[40a] and graphitized carbon fiber electrodes.[40b] The spectrum of the de-lithiated electrode after a second lithiation cycle (Figure S17b) shows features arising from both the semiquinone and catecholate forms indicating a limited reversibility of the reaction, supporting the conclusions drawn from the sXAS data. Furthermore, a low-frequency band (560 cm^{-1}) is detected in the Cu–MOF reference spectrum and the de-lithiated sample that disappears upon lithiation. It is tentatively assigned to a Cu–O stretch as discussed in more details in the Supporting Information.

Determining the Cu oxidation state from FTIR spectroscopy is more challenging than with sXAS. In addition to being sensitive to both the metal oxidation state and the identity of the O-containing ligand, the frequencies of Cu–O modes appear at very low frequencies beyond the experimentally accessible range in our setup. Cu–O bonds in amino acids, for example, are expected to appear below 400 cm^{-1}.[41] On the other hand, the Cu–O modes in a Cu benzene-1-3-5-tricarboxylate MOF were reported at 449 and 505 cm^{-1}.[42] This band is not present in the linker precursor spectrum, supporting this assignment (Figure S17b). As the Cu center is reduced, the Cu–O vibrational frequency is expected to redshift, and we hypothesize that as this happens in the lithiated sample, the frequency moves beyond the lower cut-off of our wavenumber range.

In summary, based on the sXAS results it can be stated that the copper ion is reduced during lithiation in the selected voltage window, but not completely, since both Cu^+

and Cu^{2+} were always observable. Furthermore, FTIR experiments indicate a possible reversible redox activity of the linker molecule, which might explain the gap between practical and theoretical capacity calculated by one electron per unit. However, to clearly state the exact and potential resolved mechanism further in situ studies need to be performed, which are not in the scope of this publication.

In addition to sXAS and FTIR studies, structural changes during lithiation were investigated via in situ XRD. For this purpose, flake-type $Cu_3(HHTP)_2$ was considered and analyzed, since changes along the c-axis of the stacked structure were expected to be more visible compared to the rod-like MOF due to the clearer nature of the 001 reflection (compare Figure 1c,d). Furthermore, it is assumed that the Li^+-ion storage mechanism and associated structural changes should not severely differ between both morphologies, especially at low scan rates, which are mandatory for in situ XRD experiments.

Figure 3 shows the XRD patterns recorded during the second cycle of the CV experiment as well as the corresponding cell voltage and current profiles. To the best of our knowledge, this is the first time in situ XRD has been used to investigate structural changes during the lithiation process in this class of 2D MOFs. It can be clearly seen that there is a significant shift of the *001* reflection to lower diffraction angles during lithiation, whereas the low-angle (*hk0*) reflections do not change in position. Starting at ≈2.8 V, the *001* reflection shifts from 27.3° to 25.6° 2 theta at ≈2.0 V indicating an expansion of the interlayer distance. At cell voltages below 2.0 V the reflection seems to remain at this value correlating well with the anodic peak between 2.0 V and 3.0 V (compare Figure 2b). During de-lithiation, the *001* reflection shifts back to 27.3° between 2.7 and 3.5 V (corresponding to the anodic peak in the CV, compare Figure 2b), which demonstrates the reversibility of the structural changes. Having a closer look at the *001* shift and taking the Bragg equation into account, the interlayer distance seems to only increase from 3.26 Å to 3.48 Å (+ 7 %). However, the effective ionic radius of a Li^+ is 0.9 Å without any solvation shell.[43] Based on the calculated values, the expansion of the MOF structure might not originate from a typical intercalation of the Li^+ ions directly between the MOF sheets. It seems more likely that the Li^+ ions migrate and accommodate in the MOF pores (diameter of >21 Å) close to the active redox centers and with that, the interlayer distance increases by repulsion effects between the Li^+ ions. The experiment clearly shows the widening of the structure during lithiation, which cannot be caused by only adsorption processes on the particle surface. Therefore, the widening can be interpreted as a kind of "insertion" process, although the precise crystal structure of lithiated MOF remains unclear. To get a deeper understanding of the mechanism and structural changes, the structural properties of the MOF itself as well as possible co-intercalation of solvent need to be understood in more detail. Nevertheless, the in situ XRD shows a clear hint for ongoing "insertion" process.

In contrast to the origin of electrochemical activity, the morphology and corresponding surface properties have an impact on the kinetics of electrochemical reactions. To analyze the property-performance relationships, kinetic investigations of both different morphologies were conducted via constant current cycling experiments, CV, and electrochemical impedance spectroscopy.

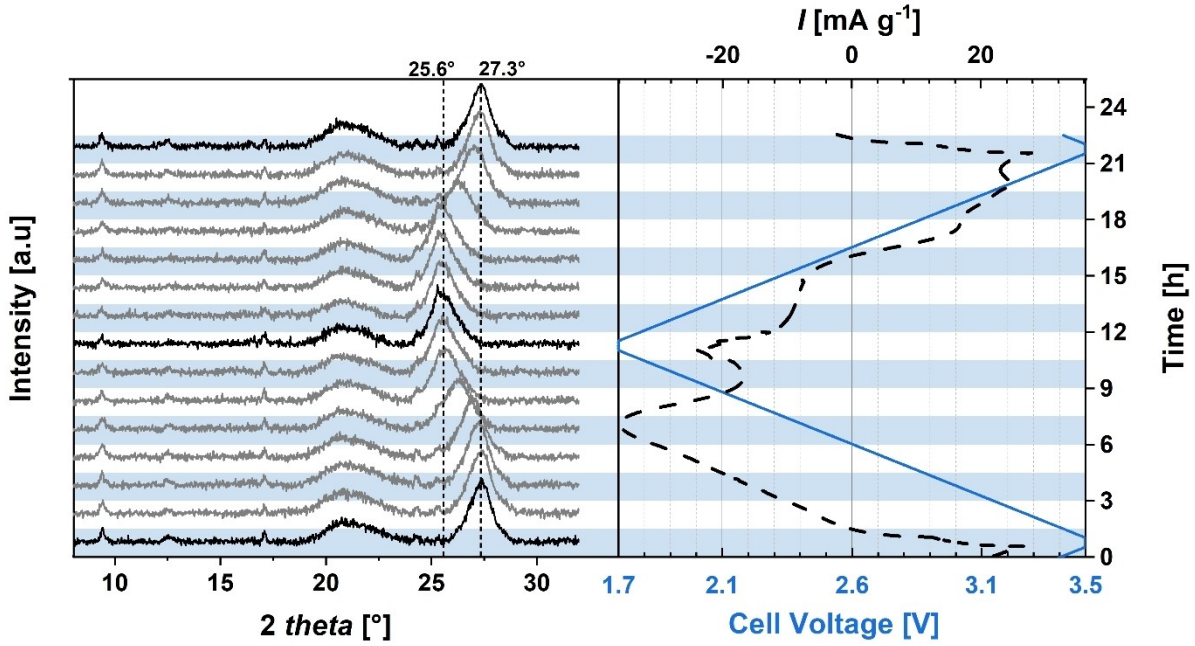

Figure 3. In situ XRD patterns (left) of flake-like $Cu_3(HHTP)_2$ as well as current and cell voltage profiles versus time (right) of the second cyclic voltammetry scan for the $Cu_3(HHTP)_2$ | | Li metal (two-electrode configuration; electrolyte: 1 M LiTFSI in EC : EMC 3 : 7 by weight) cell cycled between 3.5 V and 1.7 V at RT. The blue and grey shadows correspond to the time slot of each XRD pattern made during CV (90 min per scan).

Figure 4 shows a constant current cycling experiment for both morphologies in which the specific current was varied between 100 mA g^{-1} and 2000 mA g^{-1} for each 10 cycles after 20 initial cycles at 100 mA g^{-1}. In comparison, the flake-type MOF shows a higher capacity (≈100 mAh g^{-1}) at 100 mA g^{-1} than the rod-like material (≈60 mAh g^{-1}). With increasing current, the absolute difference in specific de-lithiation capacity between flake-like and rod-like $Cu_3(HHTP)_2$ changes only slightly. However, when normalized values are considered (Figure 4b), one can see that the flake-type MOF outperforms its rod-like analogue with increasing specific currents. This is visible most drastically at 2000 mA g^{-1} (≈20 C) where flake-like $Cu_3(HHTP)_2$ retains 20 % more of its original capacity. When reducing the current density back to the initial value of 100 mA g^{-1}, rod-like $Cu_3(HHTP)_2$ retains a greater percentage of its original capacity. Besides kinetic aspects, a stronger fading for the flake-type particles can be observed, especially in the first 20 cycles. Considering the material properties, these observations match the previous assumptions that the enhanced pore accessibility of the flake-like $Cu_3(HHTP)_2$ enables faster (de)intercalation kinetics. However, this does not explain the overall greater Li^+ ion storage capacity and the stronger fading of the flake-type MOF. To further prove this observed behavior, additional CV and impedance spectroscopy experiments were performed.

Cyclic voltammetry is a powerful tool to analyze the observed kinetics in more detail. Both synthesized materials were cycled in a potential window from 1.7 V to 3.5 V vs. Li|Li^+ at different scan rates. After the initial ten cycles, the scan rate was increased after each fifth cycle from 0.5, 1, 2, 5, 10, 20, 50 up to 100 mV s^{-1}. The results are shown in Figure S18, as expected, the current response drastically increases, and the peaks vanishes with increasing scan rate.

The current response at a specific potential $I(E)$ follows a power law dependence on the scan rate v with the exponent b and the pre-factor a.[44] In a logarithmic plot of $\log(I(E))$ vs. $\log(v)$, a and b at potential E can be determined from the y-intercept and slope, respectively.[44b,45]

$$I(E) = av^b \tag{2}$$

$$\log(I(E)) = \log(a) + b\log(v) \tag{3}$$

When the current response is proportional to the square root of the scan rate (i.e., $b = 0.5$), the process is limited by diffusion, which is typical for Faradaic processes like Li^+ ion intercalation into graphite or metal oxides. A direct proportionality to the scan rate (i.e., $b = 1$), on the other hand, is indicative of a surface-controlled process as observed in capacitors.[44b,45]

The b-values for lithiation and de-lithiation at different potentials are shown in Figure 5a and b, respectively, compared to the nominalized current response during the CV experiments at the lowest scan rate. For lithiation, one can see low b-values at higher potentials during the initial lithiation with a local minimum at ≈2.3 V vs. Li|Li^+. In general, the curves of the b-values against the potential of both morphologies are similar, but the rod-like MOF shows lower values closer to 0.5 (Figure 5a). The same is true for de-lithiation (Figure 5b). When a current peak arises during the CV (see de-lithiation between 2.2 and 2.7 V), the b-value starts to decrease, getting closer to 0.5, indicating a diffusion limitation, which is also the origin for a peak-shaped current response in a CV scan. Between 2.7 V and 3.5 V the b-value increases again. For flake-like $Cu_3(HHTP)_2$, b-values never went below 0.75 indicating that the charge storage is rarely limited by diffusion, whereas the diffusion limitation play a major role for the rod-like MOF (Figure 5a).

Furthermore, the contributions of surface and bulk processes to the overall capacity can be quantified with a method proposed by Ardizzone et al.[46] The faster a

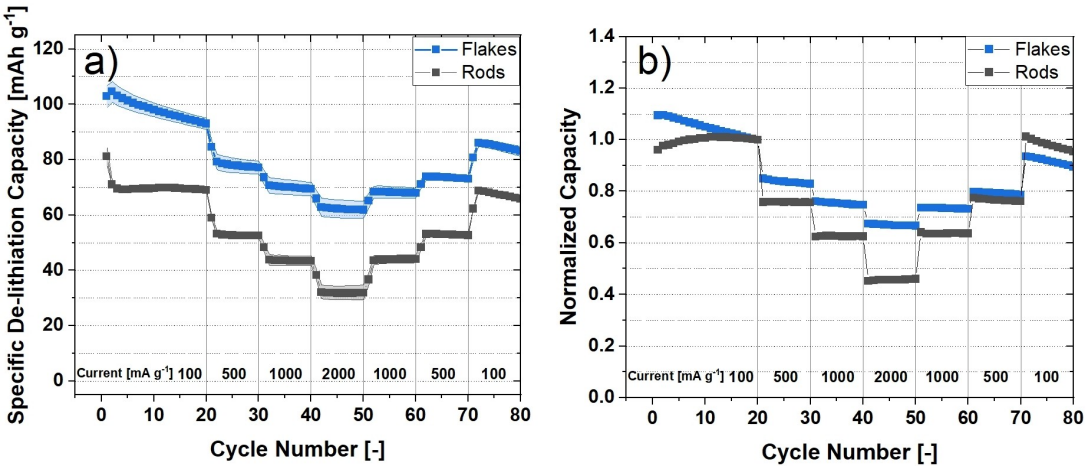

Figure 4. Constant current cycling data of rod-like and flake-like $Cu_3(HHTP)_2$||Li metal cells (three-electrode configuration; WE: $Cu_3(HHTP)_2$; CE and RE: Li metal) from 1.7 V to 3.5 V vs. Li|Li^+ at specific currents from 100 mA g^{-1} to 2000 mA g^{-1} with the electrolyte 1 M LiTFSI in EC:EMC 3:7 by weight. a) Specific de-lithiation capacity and b) normalized capacity (normalized to the 20th cycle). Error margins as calculated from the standard deviation of at least three cells. Using the theoretical capacity of 96.5 mAh g^{-1}, a specific current of 100 mA g^{-1} corresponds to ≈1 C.

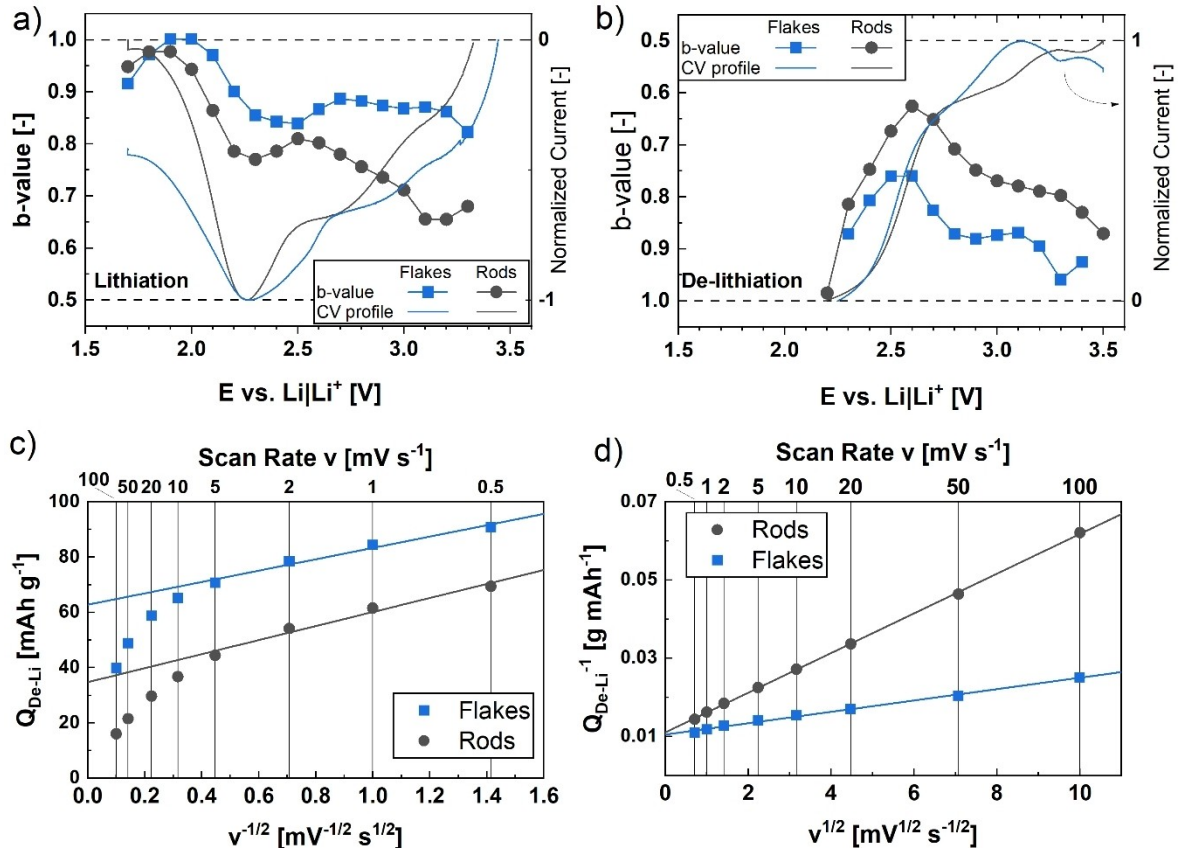

Figure 5. Analysis of cyclovoltammetry results. a), b) *b*-values obtained from linear fits of $\log(I(E))$ vs. $\log(\nu)$ from for scan rates $\nu \leq 10\ mV\,s^{-1}$ (5 data points) and current responses (CV profiles at $0.5\ mV\,s^{-1}$) for lithiation (a) and de-lithiation (b) of both MOF morphologies. c), d) Linear plots of de-lithiation capacity vs. inverse square root of the scan rate (c) and inverse capacity vs. square root of scan rate (d) to determine (c) the surface-controlled capacity (Q_S) and (b) the total capacity (Q_T) using Equations (4) and (5), respectively.

material is charged/discharged (i.e., the higher the scan rate), the less charge can actually be stored (Figure S19).

This is because the diffusion-limited processes responsible for the contribution of the bulk material to the overall capacity are too slow to keep up; hence, the faster surface-controlled contributions become dominant. At infinitely high scan rates only surface-controlled processes remain, whereas at infinitely low scan rates the sum of both surface- and bulk-controlled processes contributes to the (maximum possible) total capacity. The surface-controlled capacity (Q_S) as well as the total capacity (Q_T) can be obtained from the y-intercepts of the linear plots Q vs. $\nu^{-1/2}$ and Q^{-1} vs. $\nu^{1/2}$, respectively, as this corresponds to an extrapolation of $\nu \to \infty$ and $\nu \to 0$ (Figure 5c, d).[47]

$$Q = Q_S + k_1 \frac{1}{\sqrt{\nu}} \tag{4}$$

$$\frac{1}{Q} = \frac{1}{Q_T} + k_2 \sqrt{\nu} \tag{5}$$

$$Q_T = Q_S + Q_B \tag{6}$$

where Q_B is the bulk-controlled capacity and k_1 as well as k_2 are constants.[47] In practice, if the scan rate is increased indefinitely, the capacity will vanish, eventually leading to a sharp decline of Q vs. $\nu^{-1/2}$ at small $\nu^{-1/2}$.[48] In this case, this occurred for scan rates $\nu > 5\ mV\,s^{-1}$ which corresponds to (dis)charging times of less than 6 minutes.

The capacity contribution of surface-controlled processes differs substantially between the two morphologies, being nearly twice as high (in both absolute and relative terms) for flake-like $Cu_3(HHTP)_2$, as shown in Figure 5c. This confirms the general trend from the *b*-value analysis and is in line with the results from the physisorption experiments which showed that the flake-like morphology was more porous and offered an increased surface area.

However, assuming a surface-controlled adsorption mechanism as typical for capacitors, the capacity or capacitance should be dependent on the overall surface area of both morphologies, even at low rates. But, as can be seen in Figure 5d, both morphologies would achieve almost the same capacity of $95\ mAh\,g^{-1}$ (compare Table 1, similar to theoretical capacity) at infinite small scan rates. Considering the three times higher surface area of the flake-like compared to rod-like MOF (see Figure 1e,f), the capacity in a surface-driven double-layer charge storage mechanism only should be theoretically three times higher for the flake-like morphology, even at low scan rates. Since this is not the case, the results demonstrate, that the limitation of the rod-

Table 1: Summarized results from the data presented in Figure 5.

	Total capacity Q_T [mAh g^{-1}]	Surface-controlled capacity Q_S [mAh g^{-1}]	[%]	Bulk-controlled capacity Q_B [mAh g^{-1}]	[%]
rod-like $Cu_3(HHTP)_2$	90.4	34.8	38.5	55.6	61.5
flake-like $Cu_3(HHTP)_2$	95.2	62.8	66.0	32.4	34.0

like morphology in terms of capacity and rate capability originates from the accessibility of the active redox center and with that, from the diffusion inside or into the bulk.

Besides different kinetic aspects, the cycling experiments in Figure 4 showed a stronger fading for the flake-type MOF. Long-term constant current cycling measurements at 100 mA g^{-1} showed that rod-type $Cu_3(HHTP)_2$ also starts fading after 20 cycles (see Figure S20). However, *post mortem* analysis after 100 cycles clearly demonstrated that the morphology of both MOFs is still present (Figure S21 and S22). Impedance spectroscopy studies at different potentials were performed to get deeper insights into the kinetics and potential-resolved charging storage mechanisms and to understand the stronger fading of the flake-type $Cu_3(HHTP)_2$ in the first cycles. For this purpose, MOF-based electrodes of both morphologies were cycled in constant current experiments with a current of 100 mA g^{-1}. Each 10th cycle, alternating current (AC) impedance was measured in potential intervals of 25 mV after applying a constant potential step for 10 min at each potential. 74 impedance measurements (0.025 V steps, 1.7–3.5 V) for each morphology and every 10th cycle were performed. The impedance data, shown as a Nyquist plot in Figure S23, was used to calculate the real portions of the capacitance (C_{real}) as well as the phase angle. By a simplified consideration of the electrode as a pure capacitor neglecting severe side reactions and focusing on low frequencies, correlations of the real part of the capacitance and the phase allow general statements about charge storage mechanisms.[45c,49] The full data for both morphologies of the 10th, 30th and 50th cycle can be seen in the Supporting Information (Figure S23 and S24).

Figure 6a and b show a 3D Bode plot of the phase angle φ vs. the independent frequency and independent potential vs. Li|Li$^+$ for flake-like and rod-like $Cu_3(HHTP)_2$ during

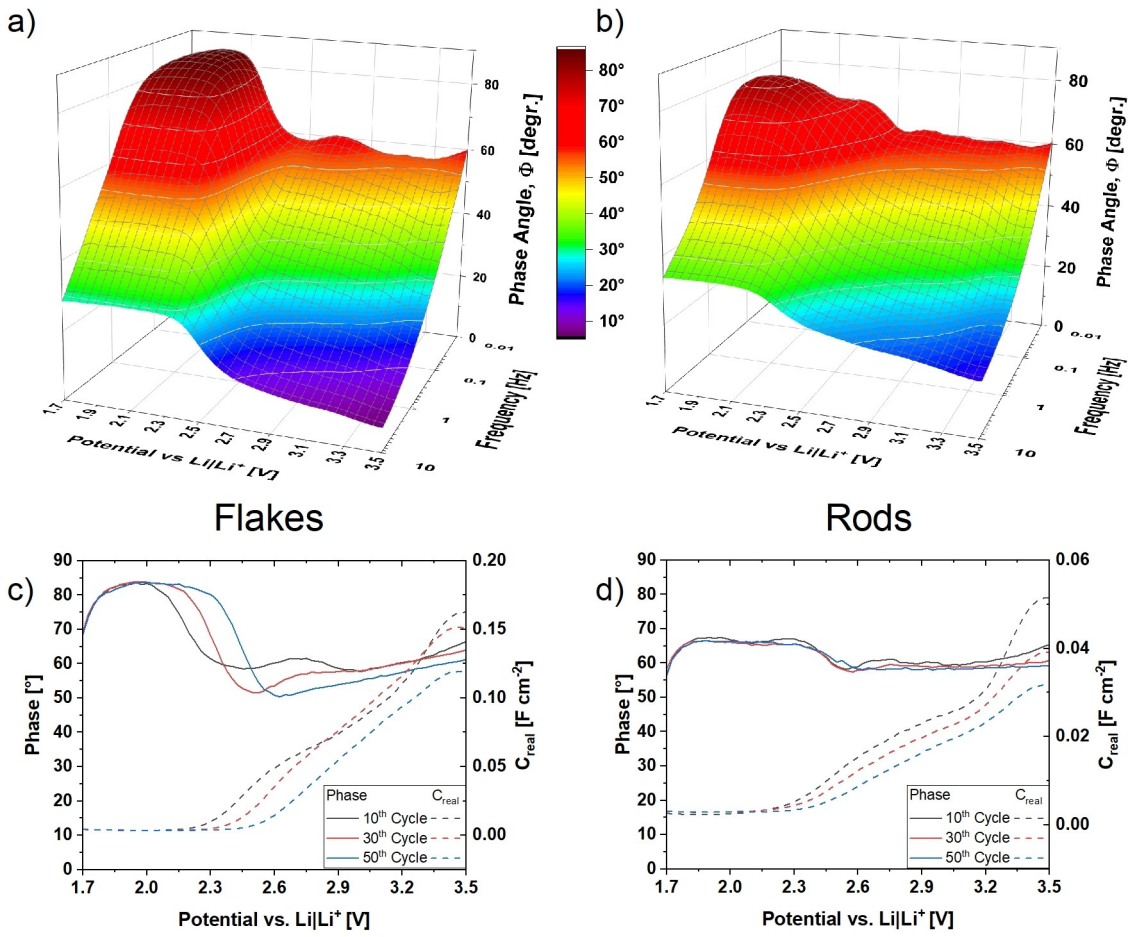

Figure 6. 3D Bode plot of the phase angle (φ) vs. frequency vs. potential vs. Li|Li$^+$ for flake- (a) and rod-like(b) $Cu_3(HHTP)_2$ after 10 cycles. (c–d) Phase angle (solid line) and area-normalized capacitances (dashed lines) vs. potential vs. Li|Li$^+$ at 5 mHz for flake-like (c) and rod-like (d) particles at 10th, 30th and 50th cycle.

de-lithiation after 10 cycles. The phase angle is defined by the cotangent of the real and imaginary components of impedance and can give insight into the kinetics. A value of 90° is equal to a capacitive response with only contributions of the real impedance, 0° is caused by pure resistive behavior, whereas a value of 45° (equal real and imaginary components of impedance) indicates a diffusion-limited process.[44a] For both morphologies, a phase angle of ≈80° is observed at low frequencies for the potential range of 1.7 V–2.4 V vs. Li|Li$^+$, which decreases during further de-lithiation to ≈60°. In earlier studies,[45c,49] a value of 60° was correlated with a so-called "pseudocapacitive" behavior, which means a charge-transfer process with low diffusion limitations.[45c,49] At higher frequencies, the course of the phase angle vs. potential remains similar but decreases drastically to lower values of <30°, thus, demonstrating a more resistor-like behavior at frequencies above 1 Hz. This strong drop is expected when it comes to materials which are not dominated by only a double-layer charge storage mechanism.[49] A closer look at a low frequency (5 mHz) is illustrated for both morphologies in Figure 6c and d. Additionally, the real capacitance is shown, which provides information of the stored charge. For both morphologies, it can be clearly seen that at ≈2.5 V the capacitance increases in parallel with the drop of the phase angle, thus, indicating that a negligible amount of charge is stored as pure capacitor-like double layer (1.7 V–2.4 V). At higher potentials the curve of the capacitance and phase angle clearly correlates with the results from the potentiostatic investigation. During cycling (10th to 50th cycles) changes are mostly observable for flake-like MOFs (Figure 6c). The region of the capacitor-type behavior increases, whereas the phase angle decreases in the electrochemical active region (2.5 V–3.5 V vs. Li|Li$^+$). Furthermore, a local maximum of the phase angle at 2.6 V in the 10th cycle for the flake-like morphology can be observed, demonstrating a low diffusion limitation. However, during cycling, this maximum disappears. For the rod-like MOF (Figure 6d), no clear local maximum with an increased phase angle at 2.6 V is observable. Furthermore, almost no changes of the phase angle are visible between the 10th and 50th cycle. The difference of the stable phase angle and capacitance behavior for flake- and rod-type MOF is in agreement with the observed different fading of both morphologies. The flake-type $Cu_3(HHTP)_2$ shows better kinetics but also a stronger fading of the capacity which correlates with the changes in the phase angles. This might be caused by some increased irreversible reactions and decomposition of the flake-type MOF during cycling due to the high surface area, subsequently slowing down the diffusion to the redox active sites.

In summary, the impedance analysis of the phase angle at different potential points out that both materials show high kinetics in the redox active potential window (from 2.5 V–3.5 V vs. Li|Li$^+$) for low frequencies and a lowered diffusion limitation indicated by a phase angle of ≈60°. Furthermore, observable processes with a "pseudocapacitive" behavior of the flake-type morphology seems to disappear during cycling correlating with the stronger fading of flake-type MOF.

The conclusions drawn from all experiments allow even more insight into about the diffusion ways of Li$^+$ ions to the active redox centers. Taking the TEM investigations on $Cu_3(HHTP)_2$ by Hoppe[17a] and Day et al.[25] into account, demonstrating hexagonal pore channels oriented parallel to the long side of the rod-like particles and perpendicular pore channels to the particle faces for the flake-like particles, a clearer picture of the insertion process for porous MOFs can be drawn. Considering the diffusion-limited process for rod-like compared to flake-like $Cu_3(HHTP)_2$, it seems that the diffusion for Li$^+$ ions is only possible along the growth direction of the rod-like particles (Figure 7). This seems to be the only way to explain the diffusion limitation, since the footprint/base of the rod and, hence, the pore accessibility is very small compared to the flakes. For the flat flake-like particles, a high number of open pores as well as a perpendicular pore direction cause short diffusion ways and allow a high rate capability indicating that Li$^+$ ions access from the top and bottom of the particles. These properties and behavior caused by highly accessible open

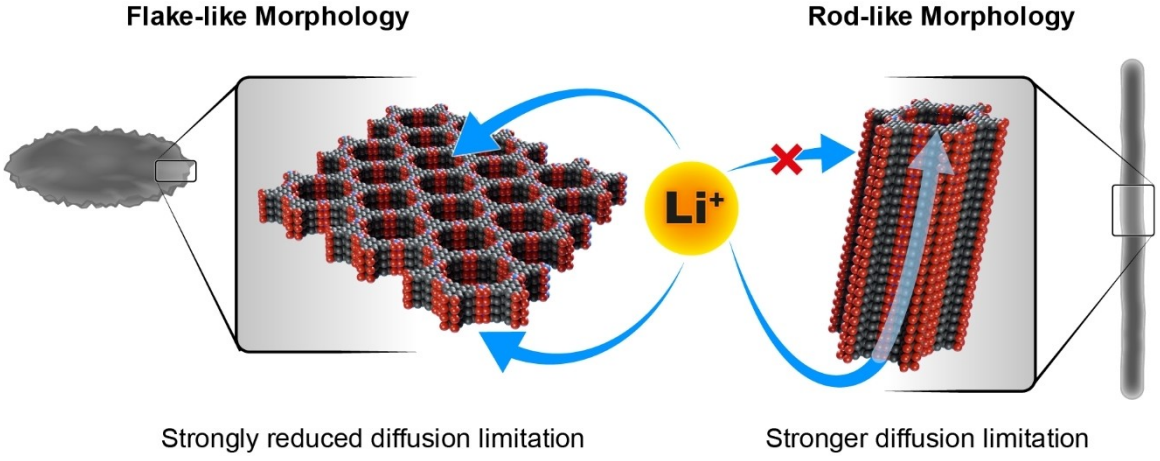

Figure 7. Scheme for assumed Li$^+$-ion diffusion path during lithiation for two different morphologies.

pores for Li^+ ions help to overcome a diffusion limitation for a Faradaic process.

Conclusion

The Li^+-ion storage mechanism and kinetics in 2D MOFs with same composition ($Cu_3(HHTP)_2$) but two different morphologies, flake- and rod-like shaped particles, were evaluated to investigate the impact of the particle morphology of MOFs on electrochemical energy storage. The flake-like microporous MOF possesses a higher total surface area compared to rod-like particles, but both showed almost similar electrochemical response in an optimized potential window (1.7–3.5 V vs. $Li|Li^+$) for cyclic voltammetry experiments at low scan rates. Ex situ sXAS proved a reversible redox activity of Cu^{2+} to Cu^+ during lithiation and thus a Faradaic process. An additional redox activity of the organic linker molecules was observed in FTIR spectra and sXAS. In situ XRD experiments of flake-like $Cu_3(HHTP)_2$, demonstrated a widening of the structure along the c-axis during lithiation. However, the widening cannot be explained by an intercalation process between the sheets of Li^+ considering the larger radius of the Li^+ ions. This behavior could be caused by an insertion process of Li^+-ions via the open pore system instead of intercalation causing Li^+ ion repulsion inside the pores and with that, a widening of the structure.

Constant current charging, kinetic CV experiments and potential-resolved impedance spectroscopy measurements were used to investigate the influence of the morphology on the kinetics of the 2D MOF. Flake-like particles, with a pore system perpendicular to the surface, demonstrated high kinetics and negligible diffusion limitation compared to rod-like particles. Thus, with this study, we could show the importance of particle morphology for electrochemical energy storage of MOFs. Diffusion limitations of faradaic processes can be overcome by highly accessible pores and short pathways. The high crystallographic and topological variety of MOFs make them an interesting material class to further understand electrochemical processes and kinetics for ion storage.

Supporting Information

Supporting Information is available from the Wiley Online Library or from the author.

Acknowledgements

This work was funded by the MWIDE NRW as part of the project "GrEEn" (313-W044A). The authors acknowledge the kind support by the staff members of the BESSY II synchrotron facility especially the beamline scientists at the beamline U49-2_PGM1. We thank Helmholtz-Zentrum Berlin for the allocation of synchrotron radiation beamtime, Prof. Dr. Philipp Adelhelm for providing electrochemical equipment and Dr. Christian Weinberger (Paderborn University) for interpretation of physisorption data. The authors thank Marvin Oude Lansink, Debbie Berghus and Simone Casino from MEET Battery Research Center for experimental support, Dr. Karin Kleiner for advice on PXRD data refinements and Dr. Simon Dühnen for co-supervising the synthesis part. Open Access funding enabled and organized by Projekt DEAL.

Conflict of Interest

The authors declare no conflict of interest.

Data Availability Statement

The data that support the findings of this study are available from the corresponding author upon reasonable request.

Keywords: Batteries · Energy Conversion · Lithium-Ion Storage · Metal-Organic Frameworks · Particle Design

[1] a) G. Zubi, R. Dufo-López, M. Carvalho, G. Pasaoglu, *Renewable Sustainable Energy Rev.* **2018**, *89*, 292–308; b) P. Meister, H. Jia, J. Li, R. Kloepsch, M. Winter, T. Placke, *Chem. Mater.* **2016**, *28*, 7203–7217.
[2] S. Dühnen, J. Betz, M. Kolek, R. Schmuch, M. Winter, T. Placke, *Small Methods* **2020**, *4*, 2000039.
[3] L. Sun, M. G. Campbell, M. Dincă, *Angew. Chem. Int. Ed.* **2016**, *55*, 3566–3579.
[4] a) C. A. Downes, S. C. Marinescu, *ChemSusChem* **2017**, *10*, 4374–4392; b) Y. Fang, Y. Ma, M. Zheng, P. Yang, A. M. Asiri, X. Wang, *Coord. Chem. Rev.* **2018**, *373*, 83–115.
[5] a) P.-Q. Liao, J.-Q. Shen, J.-P. Zhang, *Coord. Chem. Rev.* **2018**, *373*, 22–48; b) P. Li, B. Wang, *Isr. J. Chem.* **2018**, *58*, 1010–1018.
[6] I. Stassen, N. Burtch, A. Talin, P. Falcaro, M. Allendorf, R. Ameloot, *Chem. Soc. Rev.* **2017**, *46*, 3185–3241.
[7] S. K. Bhardwaj, N. Bhardwaj, R. Kaur, J. Mehta, A. L. Sharma, K.-H. Kim, A. Deep, *J. Mater. Chem. A* **2018**, *6*, 14992–15009.
[8] a) Y. Zhao, Z. Song, X. Li, Q. Sun, N. Cheng, S. Lawes, X. Sun, *Energy Storage Mater.* **2016**, *2*, 35–62; b) G. Xu, P. Nie, H. Dou, B. Ding, L. Li, X. Zhang, *Mater. Today* **2017**, *20*, 191–209; c) Y. Xu, Q. Li, H. Xue, H. Pang, *Coord. Chem. Rev.* **2018**, *376*, 292–318; d) S. Dühnen, R. Nölle, J. Wrogemann, M. Winter, T. Placke, *J. Electrochem. Soc.* **2019**, *166*, A5474–A5482.
[9] a) R. Mehek, N. Iqbal, T. Noor, M. Z. B. Amjad, G. Ali, K. Vignarooban, M. A. Khan, *RSC Adv.* **2021**, *11*, 29247–29266; b) J. M. Wrogemann, I. A. Rodríguez-Pérez, M. Winter, T. Placke, *Frontiers of Nanoscience, Vol. 19*, Elsevier, Amsterdam, **2021**, pp. 273–325.
[10] a) J. Liu, X. Song, T. Zhang, S. Liu, H. Wen, L. Chen, *Angew. Chem. Int. Ed.* **2021**, *60*, 5612–5624; b) R. Zhao, Z. Liang, R. Zou, Q. Xu, *Joule* **2018**, *2*, 2235–2259.
[11] K. Wada, K. Sakaushi, S. Sasaki, H. Nishihara, *Angew. Chem. Int. Ed.* **2018**, *57*, 8886–8890.
[12] M. Amores, K. Wada, K. Sakaushi, H. Nishihara, *J. Phys. Chem. C* **2020**, *124*, 9215–9224.
[13] Q. Jiang, P. Xiong, J. Liu, Z. Xie, Q. Wang, X. Q. Yang, E. Hu, Y. Cao, J. Sun, Y. Xu, *Angew. Chem. Int. Ed.* **2020**, *59*, 5273–5277.

[14] M. Hmadeh, Z. Lu, Z. Liu, F. Gándara, H. Furukawa, S. Wan, V. Augustyn, R. Chang, L. Liao, F. Zhou, *Chem. Mater.* **2012**, *24*, 3511–3513.
[15] W. H. Li, K. Ding, H. R. Tian, M. S. Yao, B. Nath, W. H. Deng, Y. Wang, G. Xu, *Adv. Funct. Mater.* **2017**, *27*, 1702067.
[16] A. Mähringer, A. C. Jakowetz, J. M. Rotter, B. J. Bohn, J. K. Stolarczyk, J. Feldmann, T. Bein, D. D. Medina, *ACS Nano* **2019**, *13*, 6711–6719.
[17] a) B. Hoppe, K. D. Hindricks, D. P. Warwas, H. A. Schulze, A. Mohmeyer, T. J. Pinkvos, S. Zailskas, M. R. Krey, C. Belke, S. König, *CrystEngComm* **2018**, *20*, 6458–6471; b) M. G. Campbell, S. F. Liu, T. M. Swager, M. Dinca, *J. Am. Chem. Soc.* **2015**, *137*, 13780–13783.
[18] a) M. S. Yao, X. J. Lv, Z. H. Fu, W. H. Li, W. H. Deng, G. D. Wu, G. Xu, *Angew. Chem. Int. Ed.* **2017**, *56*, 16510–16514; b) V. Rubio-Giménez, M. Galbiati, J. Castells-Gil, N. Almora-Barrios, J. Navarro-Sánchez, G. Escorcia-Ariza, M. Mattera, T. Arnold, J. Rawle, S. Tatay, *Adv. Mater.* **2018**, *30*, 1704291.
[19] K. W. Nam, S. S. Park, R. Dos Reis, V. P. Dravid, H. Kim, C. A. Mirkin, J. F. Stoddart, *Nat. Commun.* **2019**, *10*, 380.
[20] S. Fleischmann, J. B. Mitchell, R. Wang, C. Zhan, D.-e. Jiang, V. Presser, V. Augustyn, *Chem. Rev.* **2020**, *120*, 6738–6782.
[21] S. Gu, Z. Bai, S. Majumder, B. Huang, G. Chen, *J. Power Sources* **2019**, *429*, 22–29.
[22] H. Buqa, D. Goers, M. Holzapfel, M. E. Spahr, P. Novák, *J. Electrochem. Soc.* **2005**, *152*, A474–A481.
[23] Y.-R. Lee, J. Kim, W.-S. Ahn, *Korean J. Chem. Eng.* **2013**, *30*, 1667–1680.
[24] N. Stock, S. Biswas, *Chem. Rev.* **2012**, *112*, 933–969.
[25] R. W. Day, D. K. Bediako, M. Rezaee, L. R. Parent, G. Skorupskii, M. Q. Arguilla, C. H. Hendon, I. Stassen, N. C. Gianneschi, P. Kim, *ACS Cent. Sci.* **2019**, *5*, 1959–1964.
[26] K. Momma, F. Izumi, *J. Appl. Crystallogr.* **2011**, *44*, 1272–1276.
[27] A. Le Bail, *Powder Diffr.* **2005**, *20*, 316–326.
[28] W.-H. Li, J. Lv, Q. Li, J. Xie, N. Ogiwara, Y. Huang, H. Jiang, H. Kitagawa, G. Xu, Y. Wang, *J. Mater. Chem. A* **2019**, *7*, 10431–10438.
[29] a) J. L. Rowsell, O. M. Yaghi, *Microporous Mesoporous Mater.* **2004**, *73*, 3–14; b) M. D. Allendorf, R. Medishetty, R. A. Fischer, *MRS Bull.* **2016**, *41*, 865–869.
[30] M. Thommes, K. Kaneko, A. V. Neimark, J. P. Olivier, F. Rodriguez-Reinoso, J. Rouquerol, K. S. Sing, *Pure Appl. Chem.* **2015**, *87*, 1051–1069.
[31] a) J. De Boer, B. Lippens, B. Linsen, J. Broekhoff, A. Van den Heuvel, T. J. Osinga, *J. Colloid Interface Sci.* **1966**, *21*, 405–414; b) J. De Boer, B. Linsen, T. J. Osinga, *J. Catal.* **1965**, *4*, 643–648.
[32] K. Fan, C. Zhang, Y. Chen, Y. Wu, C. Wang, *Chem* **2021**, *7*, 1224–1243.
[33] a) S. Leubner, V. E. Bengtsson, A. K. Inge, M. Wahiduzzaman, F. Steinke, A. Jaworski, H. Xu, S. Halis, P. Rönfeldt, H. Reinsch, *Dalton Trans.* **2020**, *49*, 3088–3092; b) C. S. Grange, A. J. Meijer, M. D. Ward, *Dalton Trans.* **2010**, *39*, 200–211.
[34] D.-Y. Cho, S. Tappertzhofen, R. Waser, I. Valov, *Nanoscale* **2013**, *5*, 1781–1784.
[35] J.-J. Velasco-Vélez, K. Skorupska, E. Frei, Y.-C. Huang, C.-L. Dong, B.-J. Su, C.-J. Hsu, H.-Y. Chou, J.-M. Chen, P. Strasser, *J. Phys. Chem. B* **2018**, *122*, 780–787.
[36] a) S. Saikova, S. Vorobyev, M. Likhatski, A. Romanchenko, S. Erenburg, S. Trubina, Y. Mikhlin, *Appl. Surf. Sci.* **2012**, *258*, 8214–8221; b) S. Hulbert, B. Bunker, F. Brown, P. Pianetta, *Phys. Rev. B* **1984**, *30*, 2120–2126; c) M. Grioni, J. Goedkoop, R. Schoorl, F. De Groot, J. Fuggle, F. Schäfers, E. Koch, G. Rossi, J.-M. Esteva, R. Karnatak, *Phys. Rev. B* **1989**, *39*, 1541–1545; d) S. W. Goh, A. N. Buckley, R. N. Lamb, R. A. Rosenberg, D. Moran, *Geochim. Cosmochim. Acta* **2006**, *70*, 2210–2228; e) M. Grioni, J. Van Acker, M. Czyžyk, J. Fuggle, *Phys. Rev. B* **1992**, *45*, 3309–3318.
[37] a) C. Li, Q. Yang, M. Shen, J. Ma, B. Hu, *Energy Storage Mater.* **2018**, *14*, 82–89; b) F. Frati, M. O. Hunault, F. M. De Groot, *Chem. Rev.* **2020**, *120*, 4056–4110.
[38] a) S. Urquhart, H. Ade, *J. Phys. Chem. B* **2002**, *106*, 8531–8538; b) I. Koprinarov, A. Lippitz, J. F. Friedrich, W. Unger, C. Wöll, *Polymer* **1998**, *39*, 3001–3009; c) S. G. Urquhart, A. P. Hitchcock, A. Smith, H. Ade, E. G. Rightor, *J. Phys. Chem. B* **1997**, *101*, 2267–2276.
[39] a) L. B. Zasada, L. Guio, A. A. Kamin, D. Dhakal, M. Monahan, G. T. Seidler, C. K. Luscombe, D. J. Xiao, *J. Am. Chem. Soc.* **2022**, *144*, 4515–4521; b) Z. V. Bedran, S. S. Zhukov, P. A. Abramov, I. O. Tyurenkov, B. P. Gorshunov, A. B. Mostert, K. A. Motovilov, *Polymer* **2021**, *13*, 4403.
[40] a) J. Hassoun, P. Reale, S. Panero, *J. Power Sources* **2007**, *174*, 321–327; b) S. Geniès, R. Yazami, J. Garden, J. Frison, *Synth. Met.* **1998**, *93*, 77–82.
[41] a) E. J. Baran, *Z. Naturforsch. B* **2005**, *60*, 663–666; b) G. Facchin, M. H. Torre, E. Kremer, O. E. Piro, E. E. Castellano, E. J. Baran, *Z. Naturforsch. B* **2000**, *55*, 1157–1162.
[42] N. R. Dhumal, M. P. Singh, J. A. Anderson, J. Kiefer, H. J. Kim, *J. Phys. Chem. C* **2016**, *120*, 3295–3304.
[43] R. D. Shannon, *Acta Crystallogr. Sect. A* **1976**, *32*, 751–767.
[44] a) A. J. Bard, L. R. Faulkner, H. S. White, *Electrochemical methods: fundamentals and applications*, Wiley, Hoboken, **2022**; b) H. Lindström, S. Södergren, A. Solbrand, H. Rensmo, J. Hjelm, A. Hagfeldt, S.-E. Lindquist, *J. Phys. Chem. C* **1997**, *101*, 7717–7722.
[45] a) J. Wang, J. Polleux, J. Lim, B. Dunn, *J. Phys. Chem. C* **2007**, *111*, 14925–14931; b) C. Hamann, W. Vielstich, *Elektrochemie*, Wiley-VCH, Weinheim, **1998**; c) P. Bärmann, M. Winter, J. Gonzalez-Julian, T. Placke, *Small* **2021**, *17*, 2104130.
[46] S. Ardizzone, G. Fregonara, S. Trasatti, *Electrochim. Acta* **1990**, *35*, 263–267.
[47] a) J. Liu, J. Wang, C. Xu, H. Jiang, C. Li, L. Zhang, J. Lin, Z. X. Shen, *Adv. Sci.* **2018**, *5*, 1700322; b) C. Liu, E. I. Gillette, X. Chen, A. J. Pearse, A. C. Kozen, M. A. Schroeder, K. E. Gregorczyk, S. B. Lee, G. W. Rubloff, *Nat. Nanotechnol.* **2014**, *9*, 1031–1039.
[48] V. Augustyn, J. Come, M. A. Lowe, J. W. Kim, P.-L. Taberna, S. H. Tolbert, H. D. Abruña, P. Simon, B. Dunn, *Nat. Mater.* **2013**, *12*, 518–522.
[49] J. S. Ko, C.-H. Lai, J. W. Long, D. R. Rolison, B. Dunn, J. Nelson Weker, *ACS Appl. Mater. Interfaces* **2020**, *12*, 14071–14078.

Manuscript received: March 1, 2023
Accepted manuscript online: April 17, 2023
Version of record online: May 17, 2023